Ion Transport within High Electric Fields in Nanogap Electrochemical Cells

Jiewen Xiong, Qianjin Chen, Martin A. Edwards, and Henry S. White*

Department of Chemistry, University of Utah, 315 S 1400 E, Salt Lake City, Utah 84112, United States

ABSTRACT Ion transport near an electrically charged electrolyte/electrode interface is a fundamental electrochemical phenomenon that is important in many electrochemical energy systems. We investigated this phenomenon using lithographically fabricated thin-layer electrochemical cells comprising two Pt planar electrodes separated by an electrolyte of nanometer thickness (50−200 nm). By exploiting redox cycling amplification, we observed the influence of the electric double layer on transport of a charged redox couple within the confined electrolyte. Nonclassical steady-state peak shaped voltammograms for redox cycling of the ferrocenylmethyltrimethylammonium redox couple ($FcTMA^{+/2+}$) at low concentrations of supporting electrolyte ($\leq$10 mM) results from electrostatic interactions between the redox ions and the charged Pt electrodes. This behavior contrasts to sigmoidal voltammograms with a diffusion-limited plateau observed in the same electrochemical cells in the presence of sufficient electrolyte to screen the electrode surface charge (200 mM). Moreover, steady-state redox cycling was depressed significantly within the confined electrolyte as the supporting electrolyte concentration was decreased or as the cell thickness was reduced. The experimental results are in excellent agreement with predictions from finite-element simulations coupling the governing equations for ion transport, electric fields, and the redox reactions. Double layer effects on ion transport are generally anticipated in highly confined electrolyte and may have implications for ion transport in thin layer and nanoporous energy storage materials.

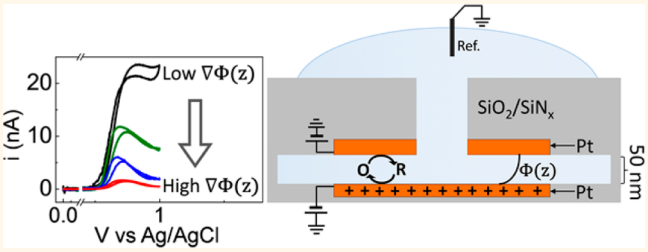

KEYWORDS: electric double layer · redox cycling · thin-layer electrochemical cells · electrostatic depletion · finite-element simulations

Nanoscale electrical energy systems, such as fuel cells,[1] batteries,[2−4] supercapacitors,[5,6] and photoelectrodes[7,8] comprising high surface area active structures, provide potential routes to high energy and power conversion/storage and are extremely attractive in research on energy storage and conversion. Understanding ion transport at the electrolyte/electrode interface and within confined geometries, between or near electrically charged electrode surfaces, is thus of fundamental importance and provides guidance for designing high performance systems. In this report, we present quantitative experimental measurements of ion transport in a fluid electrolyte confined between two Pt electrodes separated by several tens of nanometers. We demonstrate that electric double layer forces in such a highly confined geometry significantly alter the flux of charge carrying ions, thereby reducing the current to values well below that predicted from classical transport expressions.

Electrochemical experiments using macroscopic cells typically employ a high concentration of an electrochemically inert salt as the supporting electrolyte to reduce the bulk solution ohmic potential losses between the electrodes. The presence of mobile supporting electrolyte ions also leads to effective screening of the electrode surface charge, resulting in a short Debye length (λ_D, describing the extension of the electric field from the surface, typically a few nanometers or less); hence the contribution of ion migration, in response to electric double layer fields, to the overall rate of transport of inert ions and redox species is negligibly small and can generally be ignored in considering overall transport limitations within the cell. When the distance between the electrodes is comparable to λ_D, which can be achieved by either reducing the thickness of the electrolyte or the electrolyte concentration, the electrical double layer occupies a significant fraction of the distance that ions travel in carrying the current through solution; in this

* Address correspondence to white@chem.utah.edu.

Received for review June 10, 2015 and accepted July 18, 2015.

Published online July 18, 2015
10.1021/acsnano.5b03522

situation, the double layer electric fields are expected enhance or impede the flux of redox ions to the electrode surface through electromigration.[9−11]

Herein, we use lithographically fabricated, nanometer-wide thin-layer electrochemical cells (or "nanogap cells"), first reported by Lemay and co-workers,[12−14] to create a confined electrolyte in which the electrical double layer dominates ion transport behavior. In these devices two planar electrodes are separated by a thin electrolyte to exploit highly efficient redox cycling, that is, the repeated, successive reduction and oxidation of redox molecules at closely spaced electrodes, to greatly amplify the faradaic signal from a redox analyte.[15−17] Previous studies of voltammetry in ultrathin-layer electrochemical cells and using scanning electrochemical microscopy report no deviations from classic mass-transport theory.[18,19] Chen and co-workers, however, have theoretically considered the effect of the electric double layer on the electron-transfer kinetics and the mass transport dynamics of charged redox species within thin-layer cells using the finite-element simulations.[20] Bohn and co-workers have also used electric field effects in low ion strength solutions to accumulate ions in order to further enhance redox cycling at recessed ring-disk nanoelectrode arrays.[21] Using molecular dynamics simulations, Voth and co-workers predicted current inhibition due to the electric field effect on ion transport in ultrathin electrolytes at low electrolyte strength, suggesting this phenomenon would be accessible to cyclic voltammetry measurements.[22] We demonstrate that steady-state peak-shaped cyclic voltammograms are observed, and theoretically predicted, during the redox cycling of a charged redox couple (ferrocenylmethyltrimethylammonium, $FcTMA^{2+/+}$) due to double layer electric fields; moreover, the steady-state cell current decreases dramatically with decreasing supporting electrolyte concentration. Finite-element simulations coupling the governing equations of ion transport, electric fields, and the interfacial redox reactions are used to demonstrate that these unusual electrochemical phenomena arise from the interaction of the redox and electrolyte ions with the surface electric fields.

RESULTS AND DISCUSSION

The nanogap cell used in our studies is shown schematically in Figure 1a. It comprises two circular Pt planar electrodes (20 μm-diameter) separated by tens of nanometers (50−200 nm) and containing a fluid electrolyte. The cell was prepared as a Pt−Cr−Pt sandwich structure on a passivated Si wafer using lithographic patterning and electron beam evaporation, as originally described by Lemay and co-workers.[13] The sacrificial Cr layer was subsequently electrochemically etched away to leave a nanogap cell; details of cell fabrication are found in the Experimental Section and Supporting Information.

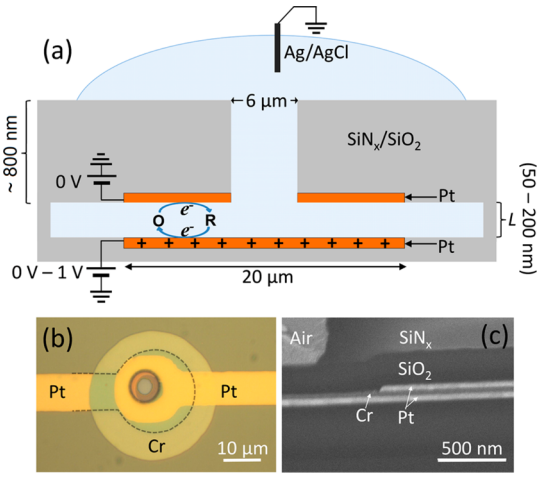

Figure 1. (a) Schematic of the nanogap electrochemical cell and redox cycling (not to scale). (b) Optical micrograph (top view). The dashed circle indicates the location of the bottom circular electrode. (c) Scanning electron micrograph (side view), where the sandwich Pt/Cr/Pt structure is indicated (1 μm slice prepared by focused ion beam milling (FEI Helios NanoLab 650)). In (a), the Ag/AgCl electrode immersed directly in the acetonitrile electrolyte corresponds to a quasi-reference electrode.

The distance, L, between the top and bottom electrodes was determined for each device using the diffusion-limited current, i_{lim}, from steady-state cyclic voltammograms for the oxidation of a neutral redox molecule, ferrocene (Fc). In these experiments, 0.1 mM Fc was dissolved in CH_3CN containing 0.10 M $TBAPF_6$ and L was computed based on the following expression for a thin-layer cell,[23]

$$i_{lim} = \frac{nFADC}{L} \quad (1)$$

In eq 1, D (2.4×10^{-5} cm^2/s) and C are the diffusion coefficient and bulk concentration of Fc, respectively; n is the number of electrons transferred per molecule (=1 for Fc); A is the overlapped area between the top and bottom electrodes, that is, the area with the central 6 μm diameter access hole excluded (current from nonoverlapping areas makes a minimal contribution to the current as these regions do not contribute significantly to redox cycling, see the Supporting Information for more details). Voltammograms recorded in the Fc solution (see the Supporting Information) display an ideal classical sigmoidal shape with a well-defined diffusion-limited current from which the cell thickness was estimated. The electrochemical cells with nominal 45, 65, and 205 nm thickness sacrificial Cr layers were determined to have thicknesses of 48 ± 7, 66 ± 9, and 210 ± 14 nm, respectively, based on measurements of ~10 cells of each thickness. The small discrepancy between the measured Cr thickness and the value of L from electrochemical measurement after Cr etching may arise from calibration errors in cell thickness measurement, (see Supporting Information) or variability in the overlapping extent between the top and

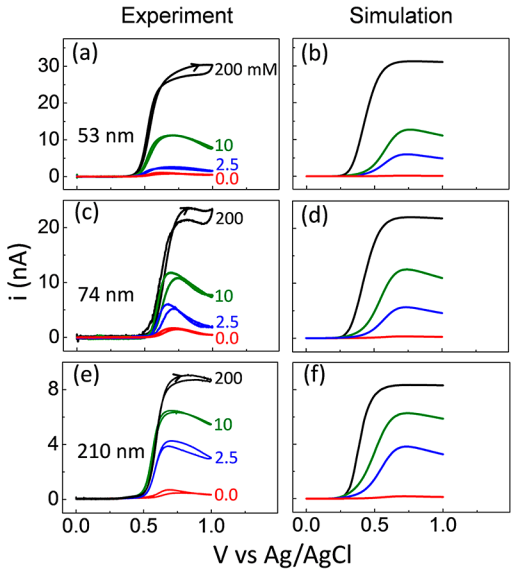

Figure 2. Experimental (a, c, e) and simulated (b, d, f) voltammetric responses of 50 μM $FcTMAPF_6$ in CH_3CN with $TBAPF_6$ at concentrations of 0, 2.5, 10, and 200 mM, respectively. Cell thicknesses were, respectively, (a, b) 53 nm, (c, d) 74 nm, and (e, f) 210 nm. The scan rate was 10 mV/s. Arrows indicate the direction of forward scans. The shifts in the apparent E^0 of the experimental voltammograms are due to the use of a quasi-reference electrode with a day-to-day variability in potential of up to 100 mV.

bottom planar electrodes (A in eq 1) resulted from imperfect mask alignment during device fabrication. The surface roughness of the Pt and Cr thin films were measured by atomic force microscopy to be ~2 and ~0.8 nm, respectively, and are believed to contribute little to this variability.

Following cell thickness calibration, solutions of 50 μM $FcTMAPF_6$ in CH_3CN containing supporting electrolyte ($TBAPF_6$) at different concentration were introduced into the thin layer electrochemical cells. Similar to Fc, $FcTMA^+$ undergoes a reversible and rapid 1-e^- oxidation ($FcTMA^+ = FcTMA^{2+} + e^-$, $E^0 \sim 0.4$ V vs Ag/AgCl). The top electrode of the cell was poised at 0.0 V vs Ag/AgCl while the bottom electrode was cycled between 0 and 1.0 V at 10 mV/s. The resulting voltammograms are displayed in Figure 2a, c, and e for thin layer cells of different thickness. As is shown schematically in Figure 1a, when the potential of the bottom electrode is sufficiently positive, $FcTMA^+$ is oxidized to $FcTMA^{2+}$, which is then transported to the top electrode where it is reduced. $FcTMA^+$ is then transported back to the bottom electrode, completing the cycle. With rapid transport this process, termed redox cycling, repeats with high frequency and offers large current enhancements, as compared to a single planar Pt electrode of the same size in a solution of the same composition. Moreover, redox cycling in a thin layer cell results in a steady-state voltammetric response.

In the presence of high concentration of supporting electrolyte (200 mM $TBAPF_6$), a conventional sigmoidal shaped, diffusion-limited current was observed for $FcTMA^+$ oxidation (black lines). These voltammograms show increasing current at decreasing cell thicknesses due to enhanced redox cycling, as predicted by eq 1. The voltammograms also display significant hysteresis on the forward and reverse scan, which is discussed further below.

At $TBAPF_6$ concentrations of 10 mM and lower, the voltammograms are peak shaped, rather than sigmoidal. As typified by the voltammogram recorded in 10 mM $TBAPF_6$ using a 53 nm thick electrochemical cell (green curve in Figure 2a), the current increases when the potential is scanned above E^0 (0.4 V) for $FcTMA^+$ oxidation and reaches a maximum value at ~0.65 V before decreasing as the potential is further increased; moreover, the $i-V$ response nearly retraces itself on the reverse sweep, indicating a quasi-steady state. This is in accord with the diffusion time of ~1 μs between the two electrodes, calculated from $\tau = L^2/2D$, where L is the cell height and D is diffusion coefficient for the redox species indicated. Note the voltammograms with 0 mM $TBAPF_6$ have a similar peak shape, although this is difficult to resolve on the scale chosen, and are thus shown on an expanded current scale in the Supporting Information. For all cell thicknesses, a decrease of current magnitude is observed as the supporting electrolyte concentration is decreased. However, this effect is more pronounced for the thinner cells.

We observed some variability of voltammetric response at low supporting electrolyte concentration, namely, the magnitude of the current may vary in different scan cycles for the same cell and experimental conditions. For example, in a 210 nm thin layer cell and when no extra supporting electrolyte was added, the current peak value at 0.65 V was ~0.53 nA for the first scan cycle. In the second scan cycle, the peak value was ~0.70 nA, which is about 32% higher (see the Supporting Information). This phenomenon is more profound at lower ionic strength and in narrower nanogap cells. We speculate that this effect may be due to adsorption of $FcTMA^+$ at the Pt surface, as discussed in the Supporting Information. However, for a given cell thickness, the voltammetric current always decreases with decreasing supporting electrolyte concentration, and the voltammograms at low supporting electrolyte concentrations are always peak shaped.

While we are confident that the peak shape characteristics of voltammetric responses for $FcTMA^+$ oxidation within the nanogap cell at different supporting electrolyte concentrations are general and reproducible, we also admit that the experimental measurement is very challenging, especially for cells with thinner thickness. A critical limitation is irreversible contact and eventual electrical shorting of the upper and lower Pt electrodes. Contact between the Pt electrodes seems to occur most often during the solution exchange process, where we place a drop of the new solution

into a PDMS cylinder atop the cell, repeating at least 10 times to ensure complete exchange of solution inside the cell with the new solution (further details available in the Experimental Section). For 210 nm thick devices, ~70% of the cells after being etched displayed electrochemical behaviors similar to that reported above, while for 53 nm thick devices, only ~20% of the cells yielded the above behavior, the remainder being shorted during the experiment.

It is surprising that all experimental voltammograms, including those in the presence of a high concentration of supporting electrolyte, display some hysteresis at the low scan rate used in these experiments (10 mV/s). We also observed hysteresis in voltammetry of $FcTMA^+$ in CH_3CN using ~25 μm diameter Pt microelectrodes; however, it was not observed in the steady state voltammetric response for Fc in the thin-layer cell employed here or at the Pt microelectrodes (see the Supporting Information). Thus, we are confident that the hysteresis in the voltammograms is not attributable to the geometry of the cell. Although the exact origin of the hysteresis is unclear, it does not obscure the observations that the forward and backward voltammetric response at low ionic strength clearly show a steady-state peak shaped feature, and that the steady-state currents decrease at lower electrolyte concentrations.

Finite-Element Simulations of the Voltammetric Response. The voltammetric response of $FcTMA^+$ oxidation within the thin-layer electrochemical cell was simulated using commercial finite-element software (COMSOL Multiphysics 4.4) as described in detail in the Supporting Information. Briefly, the transport of $FcTMA^+$, $FcTMA^{2+}$, TBA^+, and PF_6^- within the nanogap cell was described using the Nernst–Planck equation (ignoring convection)[23]

$$J_i = -D_i \nabla C_i - \frac{z_i F}{RT} D_i C_i \nabla \Phi \qquad (2)$$

where F is the Faraday constant, R is the molar gas constant, T is the absolute temperature, Φ is the potential, and J_i, D_i, C_i, and z_i, are the flux, diffusivity, concentration, and charge of the species i (either $FcTMA^+$, $FcTMA^{2+}$, TBA^+ or PF_6^-), respectively. The first and second terms on the right-hand side describe the contributions to the total flux of diffusion and migration, respectively.

Poisson's equation was used to calculate the electric potential

$$\nabla^2 \Phi = -\frac{\rho}{\varepsilon \varepsilon_0} \qquad (3)$$

where ε_0 is the vacuum permittivity and ρ is the local electrical charge density. The relative dielectric constant, ε, was set to be 6 within the Helmholtz layer (HL) which was taken to be 0.6 nm thick (d_{HL}), and 40 in bulk solution. (The effect of varying ε and d_{HL} is discussed below and in the Supporting Information). ρ is is calculated from

$$\rho = \sum z_i C_i F \qquad (4)$$

For the redox reactions at the upper and lower electrodes, $FcTMA^+ \leftrightarrow FcTMA^{2+} + e^-$, the Butler–Volmer equation was used to describe the rate of the electron-transfer reactions.

$$j = k^0[C_R \exp(\alpha f \Delta\Phi) - C_O \exp(1-\alpha) f \Delta\Phi] \qquad (5)$$

Here, j is the electron flux (= i/nFA), α is the transfer coefficient (set to be 0.5), C_R and C_O are the concentrations of reductant and oxidant at the plane of electron transfer (PET), respectively, and $f = F/(RT)$. We assume that the PET is located at the edge of the HL. $\Delta\Phi_s$ corresponds to the reaction overpotential, which equals the electrode potential minus the standard redox potential, E^0. E^0 was set to 0.4 V vs Ag/AgCl. The value of the PZC of the Pt surface influences the surface charge. For the simulations presented in the main text we assume the PZC is at 0 V; however, this does not qualitatively effect the results of the simulations; see below and Supporting Information for a more detailed discussion of the influence of the choice of PZC on the voltammetric waveshape. k^0 is the standard heterogeneous rate constant, which was set to be 5 cm/s. The faradic current results from the 1-electron oxidation of $FcTMA^+$ at the bottom electrode (scanned between 0 and 1 V) and the 1-electron reduction of $FcTMA^{2+}$ at the top electrode (held constant at 0 V), and its value was computed by integrating the flux across one of the electrode surfaces.

Simulated voltammograms corresponding to the same experimental conditions described above are shown in Figure 2 (parts b, d, and f) for comparison to the experimental voltammograms (parts a, c, and e). For all cell thicknesses, the simulated voltammograms reproduce the experimentally observed trend of decreasing current and a more peaked wave shape with lower concentrations of supporting electrolyte. Moreover, the simulated and experimental voltammograms show comparable currents and wave-shapes when the experimental variability is taken into account. Experimental voltammograms in the absence of supporting electrolyte systematically displayed slightly higher currents than their simulated counterparts, which can be explained by assuming the presence of trace ionic impurities that act to screen the electrode charge. As demonstrated in the Supporting Information, simulations performed assuming ~300 μM of an impurity 1:1 electrolyte yield voltammetric currents and wave shapes that are in quantitative agreement with the experimental observations.

The simulated concentration distribution of $FcTMA^+$ in the presence of excess supporting electrolyte (200 mM $TBAPF_6$) in a 74 nm thin layer cell is shown in Figure 3

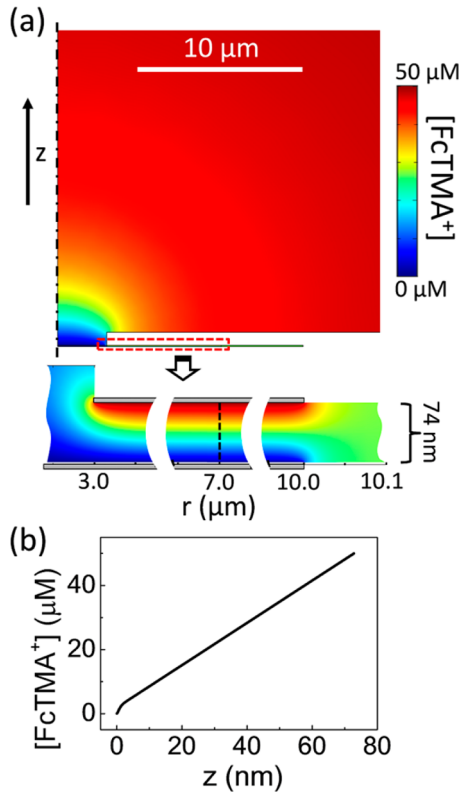

Figure 3. Plots of the concentration distribution of $FcTMA^+$ in a 74 nm cell with 200 mM $TBAPF_6$ when the potential of the bottom electrode is 1.0 V. (a) Color image featuring zoom-in of the electrode edges and center. (b) Cross section through the center of the electrode (dashed line in zoom-in of part a).

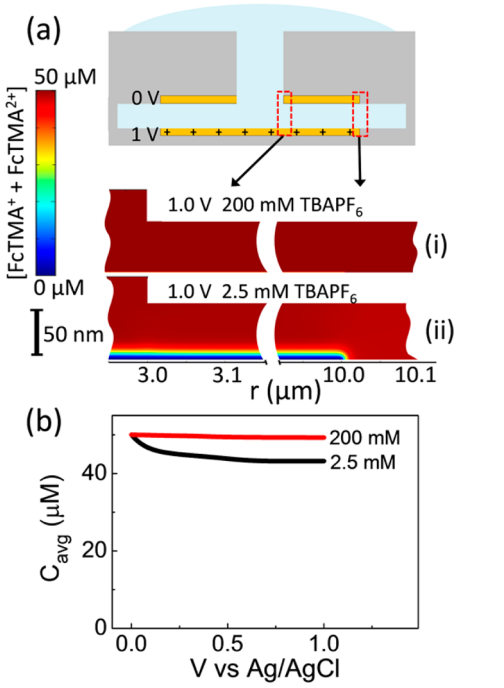

Figure 4. (a) Surface plot of the total concentration distribution of $FcTMA^+$ and $FcTMA^{2+}$ in a 74 nm thin layer electrochemical cell when the bottom electrode potential is set to 1.0 V with (i) 200 mM $TBAPF_6$ and (ii) 2.5 mM $TBAPF_6$. (b) Averaged total concentration of $FcTMA^+$ and $FcTMA^{2+}$ within the cell as a function of bottom electrode potential with different $TBAPF_6$ concentrations.

with the bottom electrode at 1 V to oxidize $FcTMA^+$ and the top electrode at 0 V to reduce $FcTMA^{2+}$. At this high ionic strength, the electrical double layer is highly compressed (λ_D = 0.5 nm), and the transport of the redox species within the cell is almost entirely diffusional. With the bottom electrode potential at 1.0 V, the concentration of $FcTMA^+$ at this electrode is essentially zero since the forward rate (first term in the Butler−Volmer equation,eq 5) is very fast and all $FcTMA^+$ ions are oxidized to $FcTMA^{2+}$. At the top electrode $FcTMA^+$ is present at the bulk concentration, 50 μM. Figure 3b shows the concentration profile computed far away from the electrode edges (r = 7 μm, dashed line in zoom-in of part a). This plot shows that the $FcTMA^+$ concentration distribution is essentially linear between the bottom and the top electrodes; a small deviation from linearity is observable in the region close to bottom electrode surface, as the fluxes within this region are influenced by electric field in the electrical double layer (λ_D = 0.5 nm). In the region of the access hole the bottom electrode does not have an electrode above it and redox cycling does not take place; thus, this region does not contribute significantly to the computed current, nor does redox processes near the edges. Calculations assuming the current density at r = 7 μm occurs at every point on the top electrode yields less than a 0.2% deviation from the full simulation (see the Supporting Information for details).

Simulations performed assuming the presence of 200 mM supporting electrolyte show that the sum of the concentrations of $FcTMA^+$ and $FcTMA^{2+}$ is essentially equal to the bulk concentration of $FcTMA^+$ (50 μM), as it would be if the mass transport was purely diffusive. This is shown in Figure 4a(i) when the bottom electrode is at 1.0 V and is indicated by the red line in Figure 4b, which presents the *average total redox concentration in the volume* between the electrodes. Note, the simulation predicts ~1% depletion of redox species within the very thin double layer (λ_D = 0.5 nm) at the bottom electrode surface, but has an insignificant effect on the total concentration within the nanogap cell or the voltammetric response. In contrast, when the supporting electrolyte is low (2.5 mM, λ_D ~5 nm), depletion of the redox molecules is observed close to the bottom electrode. This is visible in Figure 4a(ii) as a blue/green region, indicating that $FcTMA^+$ and $FcTMA^{2+}$ ions are largely excluded from the double layer region. The average total concentration of $FcTMA^+$ and $FcTMA^{2+}$ between the electrodes as a function of the applied potential is presented as the black line in Figure 4b. The depletion of redox species at 2.5 mM $TBAPF_6$ increases gradually as the potential is increased and levels off at potential of ~0.50 V with a limiting total concentration ~43 μM, implying a 15% reduction in the number of the redox

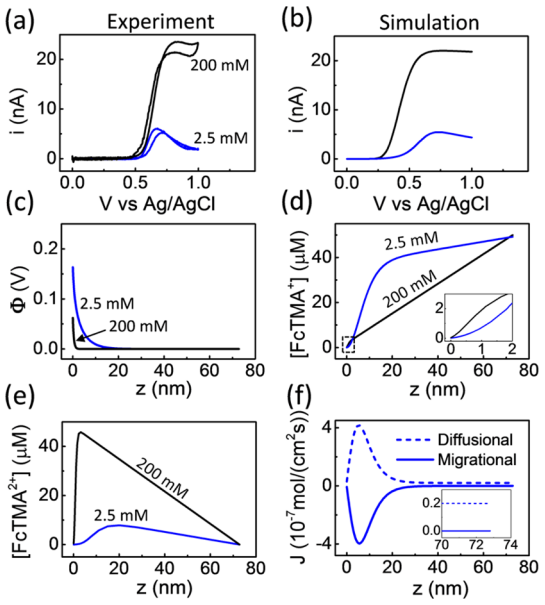

Figure 5. (a) Experimental and (b) simulated cyclic voltammograms for 50 μM FcTMA$^+$ oxidation in a 74 nm thin layer cell with TBAPF$_6$ concentrations of 2.5 and 200 mM. Simulated (c) potential profiles, concentration distributions of (d) FcTMA$^+$ and (e) FcTMA^{2+} across the cell (dashed line in Figure 3a), in the same system, at the bottom electrode potential of 0.7 V. (f) Diffusional and migrational fluxes of FcTMA$^+$ across the cell with 2.5 mM TBAPF$_6$ also at 0.7 V; inset shows fluxes close to the top electrode. (Diffusional and migrational fluxes of FcTMA$^+$ with 200 mM TBAPF$_6$ concentration are presented in the Supporting Information.) Note: potential distribution in HL not shown in part (c).

ions (FcTMA$^+$ and FcTMA^{2+}). The experimental (a) and simulated (b) voltammograms for these two systems at 200 mM and 2.5 mM TBAPF$_6$ are reproduced in Figure 5, and both show that the voltammetric current with 2.5 mM TBAPF$_6$ is ~1/5 of that with 200 mM TBAPF$_6$. Thus, phenomena other than simple redox depletion are responsible for the decrease in current with decreasing supporting electrolyte concentration.

In 2.5 mM TBAPF$_6$, the voltammetric current reaches its maximum value at ~0.7 V before it starts to drop with further increases in potential, and it is at this potential that we examined the concentration profiles across the cell. As expected, for both supporting electrolyte concentrations the majority of the potential drop occurs within the Helmholtz layer (HL) as can be seen in Figure 5c. At 200 mM TBAPF$_6$, the potential at the PET is 0.06 V, and decreases rapidly to 0.0 V ~1 nm away from the PET. At 2.5 mM TBAPF$_6$, the potential at the PET is 0.16 V, and decreases gradually to 0.0 V at ~20 nm from the PET. Figure 5d and e shows the simulated concentrations of FcTMA$^+$ and FcTMA^{2+} at the r = 7 μm cross-section between the electrodes (dashed line, Figure 3a). In all cases, the concentrations are linear beyond the double layer region of the bottom electrode, indicating that mass transport outside the double layer occurs by diffusion. For the 200 mM electrolyte, the linear region begins ~1 nm from the bottom electrode; whereas, for 2.5 mM TBAPF$_6$ it begins ~20 nm away. That mass transport is governed by diffusion beyond the double layer is confirmed in Figure 5f, which shows the two simulated components of FcTMA$^+$ flux across the domain for 2.5 mM TBAPF$_6$.

Within the double layer at the bottom electrode, there is an appreciable electric field which repels both positively charged redox species. For FcTMA^{2+}, migration in the double layer occurs in the same direction as the net flux of this ion (bottom to top electrode). For FcTMA$^+$, the net flux is directed toward the bottom electrode whereas migration acts in the opposite direction, as can be seen in Figure 5f. FcTMA$^+$ is repelled from the bottom electrode resulting in a nearly zero concentration at the bottom electrode surface and an increasing concentration nearer the top electrode (Figure 5d). Electromigration reflects the product of the local redox concentration (Figure 5d) with the local electric field (the negative of the gradient of Figure 5c); the opposing trends of these two components result in the migrational flux of FcTMA$^+$ being zero at the electrodes and achieving a maximal magnitude at ~8 nm from the electrode surface. Note that although the total flux is equal at all points, the diffusional flux, which is proportional to the concentration gradient, increases from zero to a peak value at ~8 nm away from the bottom electrode, and then decreases again.

Interestingly, we note that the average concentrations of the two redox species are unequal at the low supporting electrolyte concentration, with a much higher proportion residing in the +1 form (7:1 FcTMA$^+$:FcTMA^{2+}); this suggests that the transport of FcTMA$^+$ to the bottom electrode is indeed the rate limiting step as will be shown in detail below. Such unequal average concentrations of the two halves of the redox pair also occurs in situations where the two species have different diffusion coefficients.[24]

To understand the peak shaped cyclic voltammograms at low supporting electrolyte concentration, it is important to consider the diffusional and migrational components of mass-transport, as illustrated in Figure 6. The simulated voltammogram (Figure 6a) for 50 μM FcTMA$^+$ oxidation in a 74 nm cell with 2.5 mM TBAPF$_6$ shows a maximal current at around 0.7 V. The contributions to the current of FcTMA$^+$ diffusion and migration at the bottom electrode are presented in Figure 6c as a function of applied potential. These components act in opposing directions and have magnitudes that are in general much larger than the current (i.e., the sum of the two transport components).

In sections I and II labeled on Figure 6c, no net current flows as the potential is far below E^0 (0.4 V). However, concentration polarization occurs (green/black curves, part b) with the positively charged electrode repelling the positive FcTMA$^+$. This polarization causes a steady-state where the diffusional and migrational fluxes are equal but opposite in sign and thus

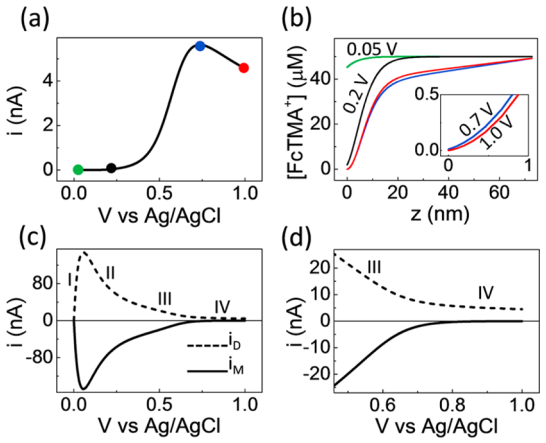

Figure 6. (a) Simulated cyclic voltammogram for 50 μM FcTMA$^+$ oxidation in a 74 nm cell with 2.5 mM TBAPF$_6$. (b) Concentration distribution of FcTMA$^+$ across the cell (dashed line in Figure 3a) at potentials of 0.05, 0.2, 0.7, and 1.0 V applied to the bottom electrode. (c) Diffusional and migrational currents of FcTMA$^+$ at the bottom electrode as a function of the potential applied to the bottom electrode. (d) Zoom-in of region (IV) in (c).

perfectly balanced, that is, no net flux (current) occurs. As the potential of the bottom electrode is increased the electric field increases, leading to an increase in concentration polarization, as can be seen comparing the green curve (50 mV) to black curve (200 mV) in Figure 6b. The migrational flux away from the bottom electrode, which is proportional to the concentration and the electric field, initially increases with increasing potential/electric field (section I in Figure 6c); however, as the surface concentration tends to zero it begins to diminish (section II).

When the bottom electrode voltage is above E^0, FcTMA$^+$ oxidation occurs in appreciable amounts and a current is observed. The rate constant for oxidation increases with increasing potential as described by the Butler–Volmer equation (eq 5) and in region III this is the dominant factor causing the increasing current with voltage. However, once the potential is high enough the oxidation reaction goes to completion and the surface concentration of FcTMA$^+$ is essentially zero (see inset of Figure 6b); at these potentials mass transport dominates the electrode current (region IV). With zero surface concentration the surface migrational flux must be zero, as indicated in Figure 6d which shows a zoomed in region of the surface flux of FcTMA$^+$. A diffusional flux, proportional to the concentration gradient, remains as the source of all the current at the bottom electrode. The inset in Figure 6b indicates that at a higher potential (1.0 V relative to 0.7 V), the FcTMA$^+$ is repelled more strongly resulting in a lower concentration gradient at the electrode surface, and thus a lower diffusive flux (Figure 6d) and current (Figure 6a).

So far, we have successfully explained the experimental observation of current inhibition induced by the electrical field in a thin layer electrochemical cell when the supporting electrolyte concentration is low. Note that the electrostatic depletion only occurs within the electrical double layer region. Increasing the supporting electrolyte concentration narrows the electrical double layer, which results in a different voltammetric response. In particular, with excess supporting electrolyte (200 mM TBAPF$_6$), mass transport is almost diffusion controlled (see the Supporting Information for comparison). The extent to which the electric field, $-\nabla\Phi$, extends from the electrode is known as the electrical double layer and characterized by the Debye length, λ_D

$$\lambda_D = \sqrt{\frac{\varepsilon_0 \varepsilon kT}{e^2 \sum C_i z_i^2}} \qquad (6)$$

where ε and ε_0 are the relative electric permittivity of the solvent and permittivity of vacuum, respectively, k is the Boltzmann constant, and e is the elementary charge. Overall, as the supporting electrolyte concentration increases, the voltammetric current increases, eventually reaching the diffusion-limited value at high electrolyte concentrations. A peak shaped voltammogram occurs whenever the ion depletion within the double layer is significant. Simulated results for 10 and 0 mM supporting electrolyte concentration have the same form as that presented in Figures 4–6 for 2.5 mM.

Importantly, while the exact value of a simulated current may be changed by varying a parameter, none of the conclusions in this work is dependent on the exact value chosen for any parameter; this was confirmed by simulations using alternative parameters, such as the PZC, k^0, ε within the HL, and d_{HL}, in the simulations. Each has a degree of uncertainty to them. First, different values of the PZC will influence the surface charge at electrodes, resulting in different electrostatic effects between electrodes and ions, especially in low supporting electrolyte concentrations. Simulations with a series of PZC values,[25] between −0.2 and 0.2 V at 2.5 mM TBAPF$_6$ in a 74 nm cell, show that the voltammetric current increases at positive PZC and decreases at negative PZC, consistent with the expectation from electrostatics (see Supporting Information). More importantly, the peak shape feature of the voltammogram is always observed, indicating that different PZC value does not qualitatively influence mass transport. Second, the standard rate constant for FcTMA$^+$ oxidation, k^0, determines the electrochemical reaction kinetics. Simulations using different standard rate constant, 2, 5, and 10 cm/s, which have been reported in previous literature,[26] were performed. It was found that a change in the standard rate constant effects the voltammetric current near E^0 but a peaked shape is observed regardless of the chosen value of k^0. Finally, the potential drop within Helmholtz layer can be affected by relative dielectric constant, ε, within d_{HL}. If the potential drop within the compact layer is greater, by using either a

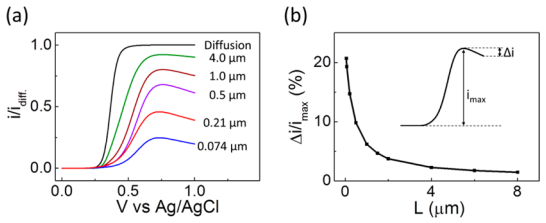

Figure 7. Simulated voltammetry of 50 μM FcTMA$^{+/2+}$ in thin layer cells of varying thickness (L = 53 nm −8000 nm) containing 2.5 mM supporting electrolyte. (a) Simulated voltammograms normalized to the diffusion-limited current (substituting L into eq 1) and (b) percentage decrease in the current from the peak current to the current at 1 V. In all cases d_{HL} = 0.6 nm, PZC = 0 V. k^0 = 5 cm/s and ε_{HL} = 6.

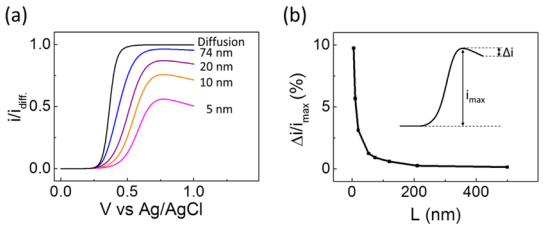

Figure 8. Simulated voltammetry of 50 μM FcTMA$^{+/2+}$ in thin layer cells of varying thickness (L = 5−500 nm) containing 200 mM supporting electrolyte. (a) Simulated voltammograms normalized to the diffusion-limited current (substituting L into eq 1) and (b) percentage decrease in the current from the peak current to the current at 1 V. In all cases, d_{HL} = 0.6 nm, PZC = 0 V, k^0 = 5 cm/s, and ε_{HL} = 6.

thicker HL or a lower dielectric constant, the effect of electrostatics between electrodes and ions will be less significant. Simulation of voltammograms in a 74 nm cell with different relative constant and HL thickness were performed and results are presented in the Supporting Information. Regardless of the value of the thickness or ε in the HL, the voltammograms still display a well-defined peak.

Dependence of Double Layer Effects on Cell Thickness. Finite-element simulations were also used to investigate in more detail the role of cell thickness, L, in controlling the voltammetric wave shape. Figure 7a shows normalized voltammograms for 50 μM FcTMA$^{+/2+}$ in 2.5 mM supporting electrolyte in thin layer cells of varying thickness (L = 53 nm −8000 nm). Figure 8a shows the same simulations in 200 mM supporting electrolyte. In general, as the thickness of the cell is increased, the normalized voltammograms tend to the diffusion-limited sigmoidal shaped voltammogram. Specifically, the wave shape becomes less peaked as the cell thickness is increased and the magnitude of the normalized current increases. Figures 7b and 8b show the percentage drop in the current following the peak current at high and low electrolyte concentrations. We observe that the decrease in current following the peak is less than 5% when L is greater than ~1.5 μm in the solution containing 2.5 mM supporting electrolyte. At higher electrolyte concentration (200 mM), the drop in current is less than 5% when L is greater than ~13 nm. Surprisingly, these cell thicknesses are still considerably larger than the Debye screening lengths in 2.5 mM (λ_D ~ 5 nm or 0.3% of 1.5 μm) and 200 mM supporting electrolyte (λ_D ~ 0.5 nm or 4% of 13 nm), indicating that double layer effects influence cell behavior over much longer distances than originally expected based on the thickness of the diffuse double layer.

Recently, Amemiya and co-workers used the same FcTMA$^{2+/+}$ couple to study the organic contamination of highly oriented pyrolytic graphite (HOPG) from ultrapure water by SECM.[26] However, only sigmoidal-shaped voltammograms (no peaks) were observed at SECM tip/electrode separations between 30 to 500 nm. Considering the similarity between the SECM tip/electrode geometry and the nanogap cells in our studies, it is surprising that a current inhibition was not observed in their study.

CONCLUSION

In this paper, we reported the influence of the electrical double layer on ion transport within nanometer wide thin-layer electrochemical cells. We have demonstrated, by both experiments and simulations, that the electrochemical behavior of a simple redox system departs from classical diffusion-only behavior when the spacing between the electrodes is on the order of 10s to 100s of nanometers. Instead of a sigmoidal $i-V$ curve, a steady-state peak shaped voltammogram was observed experimentally for FcTMA$^+$ oxidation. Current attenuation as the electrode potential is increased beyond E^0 results from the interplay of the diffusional and migrational fluxes, which are dependent on ion distribution and the electric field within the electric double layer. The current inhibition phenomenon becomes less significant as the supporting electrolyte concentration increases. The experimental results agree well with predictions from the finite-element simulations based on numerical solution of the Poisson, Nernst−Planck, and Butler−Volmer equations. The findings from this study appear to be applicable to other systems where mass transport occurs on nanometric length scales, as is increasingly the case in high performance electrochemical energy systems.

EXPERIMENTAL SECTION

Reagents. Ferrocene (Fc) (Aldrich) was purified by sublimation. Tetrabutylammonium hexafluorophosphate ($TBAPF_6$) (Aldrich) was recrystallized from absolute ethanol and dried under vacuum. Ferrocenylmethyltrimethylammonium hexafluorophosphate ($FcTMAPF_6$) was prepared by metathesis of ferrocenylmethyltrimethylammonium iodide (Alfa Aesar) with ammonium hexafluorophosphate (Aldrich) in water at ~60 °C for 1 h, followed by recrystallization from water and drying under vacuum.[9,27] Acetonitrile (HPLC grade) was used as received.

Electrochemical Measurements. A bipotentiostat Pine AFRDE5 was employed for the three-electrode voltammetric measurements, where the upper/lower electrodes of the thin-layer cell were the two working electrodes. In order to directly immerse the reference electrode into the acetonitrile solution, a chloridized Ag wire was used as a quasi-reference electrode. Note that the potential for the Ag wire quasi-reference electrode may vary by ~100 mV from experiment to experiment. All potentials reported in this paper are relative to the Ag/AgCl wire. The potentiostat was interfaced to a PC computer running custom written programs (LabVIEW 2010, National Instruments) through a multifunction data acquisition card (PCI-6040, National Instruments). All experiments were performed inside a Faraday cage at room temperature.

Nanometer Wide Thin Layer Cell Fabrication. Design and fabrication of the nanometer wide thin layer electrochemical cells shown in Figure 1 followed a method similar to that reported by the Lemay group.[12,13] Briefly, a sandwich structure consisting of (1) a 20 μm diameter, 30 nm thick circular bottom Pt electrode, (2) a 35 μm diameter sacrificial Cr layer with desired thickness of L = 45, 65, or 205 nm, and (3) a 20 μm diameter, and a 30 nm thick circular top Pt electrode, were sequentially deposited on a Si wafer (with a 500 nm thermally grown SiO_2) by electron-beam evaporation and patterned using lift-off photolithography. Film thicknesses were monitored by a quartz crystal microbalance measurement during electron-beam evaporation. Both the bottom and top electrodes were electrically connected by square conduction pads. Afterward, the device was passivated by a 1 μm thick SiN_x/SiO_2 layer using plasma-enhanced chemical vapor deposition (300 °C). Conduction pads and access holes were then etched through the passivation layer using reactive ion etcher (CHF_3/O_2 reactive ion etching in a Oxford 80 Plasma System). Figure 1b and c shows the optical micrographic top-view and electron micrographic side-view of the device at this stage of the fabrication process. Multiple devices were patterned on a single wafer which was diced into 15 mm × 6 mm chips, each containing a single electrochemical cell. A small PDMS block with a cylindrical channel (~5 mm diameter) in the center was adhered on top of the chip and served as the bulk solution reservoir containing the reference electrode, and for introducing new solutions. Additional fabrication details are presented in the Supporting Information and the original articles by Lemay and co-workers.[12,13]

After the fabrication, the middle sacrificial Cr layer was removed to generate a nanogap between the two planar electrodes. In contrast to conventional chemical wet Cr etching,[12] where the etchant solution is introduced and a small bias (10 mV) is applied between the top and bottom electrodes to monitor the etching process, we used an electrochemical etching method, where the top and bottom electrodes are shorted and a potential is applied vs a reference electrode, which is reported to significantly increase the etch rate.[28] Specifically, after introducing the Cr etchant solution (15 mM CH_3COOH, 0.10 M KNO_3, and 4 mM $Ce(NH_4)_2(NO_3)_6$), a potential of 0.75 V vs Ag/AgCl was applied to the top and bottom electrodes. A typical time-current trace during the etching process is provided in the Supporting Information. The total charge calculated from integration of the shaded area agrees well with the total amount of Cr layer estimated from evaporation (see the Supporting Information). After the complete removal of the sacrificial Cr layer, the etching solution was replaced with pure water and background voltammograms were recorded (see Supporting Information). The success rate for fabrication is strongly dependent on the device thickness. For devices with 200 nm nominal thickness, ~90% could be etched to give a clean background voltammogram; whereas for the thinnest devices (45 nm nominal thickness), the success rate was ~30%.

The solution within the cell was replaced by a new solution by placing a drop of the new solution in the PDMS cylinder to allow diffusional mixing. Quantitative exchange of one solution for another was achieved by repeating this process at least 10 times.

Conflict of Interest: The authors declare no competing financial interest.

Acknowledgment. This work was supported by the office of Naval Research (N000141211021). This work made use of University of Utah shared facilities of the Micron Technology Foundation Inc. Microscopy Suite and the Utah Nanofab sponsored by the College of Engineering, Health Sciences Center, Office of the Vice President for Research, and the Utah Science Technology and Research (USTAR) initiative of the State of Utah. The authors appreciate the support of the staff and facilities that made this work possible. This work also made use of University of Utah USTAR shared facilities supported, in part, by the MRSEC Program of the NSF under Award No. DMR-1121252. Thanks to R. Polson at Nanofab at University of Utah for assistance in preparing and imaging the sample for SEM shown in Figure 1c.

Supporting Information Available: Charge calculation for sacrificial Cr layer etching. Geometry, meshes, and boundary conditions of finite-element simulation, sensitivity analysis of the simulation parameters and fabrication details, and more information. The Supporting Information is available free of charge on the ACS Publications website at DOI: 10.1021/acsnano.5b03522.

REFERENCES AND NOTES

1. Steele, B. C. H.; Heinzel, A. Materials for Fuel-Cell Technologies. *Nature* **2001**, *414*, 345–352.
2. Long, J. W.; Dunn, B.; Rolison, D. R.; White, H. S. Three-Dimensional Battery Architectures. *Chem. Rev.* **2004**, *104*, 4463–4492.
3. Arthur, T. S.; Bates, D. J.; Cirigliano, N.; Johnson, D. C.; Malati, P.; Mosby, J. M.; Perre, E.; Rawls, M. T.; Prieto, A. L.; Dunn, B. Three-Dimensional Electrodes and Battery Architectures. *MRS Bull.* **2011**, *36*, 523–531.
4. Oudenhoven, J. F. M.; Baggetto, L.; Notten, P. H. L. All-Solid-State Lithium-Ion Microbatteries: A Review of Various Three-Dimensional Concepts. *Adv. Energy Mater.* **2011**, *1*, 10–33.
5. Chmiola, J.; Yushin, G.; Gogotsi, Y.; Portet, C.; Simon, P.; Taberna, P. L. Anomalous Increase in Carbon Capacitance at Pore Sizes Less Than 1 Nanometer. *Science* **2006**, *313*, 1760–1763.
6. Simon, P.; Gogotsi, Y. Materials for Electrochemical Capacitors. *Nat. Mater.* **2008**, *7*, 845–854.
7. Kamat, P. V.; Tvrdy, K.; Baker, D. R.; Radich, J. G. Beyond Photovoltaics: Semiconductor Nanoarchitectures for Liquid-Junction Solar Cells. *Chem. Rev.* **2010**, *110*, 6664–6688.
8. Kubacka, A.; Fernández-García, M.; Colón, G. Advanced Nanoarchitectures for Solar Photocatalytic Applications. *Chem. Rev.* **2012**, *112*, 1555–1614.
9. Zhang, Y.; Zhang, B.; White, H. S. Electrochemistry of Nanopore Electrodes in Low Ionic Strength Solutions. *J. Phys. Chem. B* **2006**, *110*, 1768–1774.
10. Belding, S. R.; Compton, R. G. Cyclic Voltammetry in the Absence of Excess Supporting Electrolyte: The effect of Analyte Charge. *J. Electroanal. Chem.* **2012**, *683*, 1–13.
11. Lingane, J. J.; Kolthoff, I. M. Fundamental Studies with the Dropping Mercury Electrode. II. The Migration Current. *J. Am. Chem. Soc.* **1939**, *61*, 1045–1051.
12. Zevenbergen, M. A. G.; Wolfrum, B. L.; Goluch, E. D.; Singh, P. S.; Lemay, S. G. Fast Electron-Transfer Kinetics Probed in Nanofluidic Channels. *J. Am. Chem. Soc.* **2009**, *131*, 11471–11477.
13. Kätelhön, E.; Hofmann, B.; Lemay, S. G.; Zevenbergen, M. A. G.; Offenhäusser, A.; Wolfrum, B. Nanocavity Redox Cycling Sensors for the Detection of Dopamine Fluctuations in Microfluidic Gradients. *Anal. Chem.* **2010**, *82*, 8502–8509.
14. Rassaei, L.; Singh, P. S.; Lemay, S. G. Lithography-Based Nanoelectrochemistry. *Anal. Chem.* **2011**, *83*, 3974–3980.
15. Singh, P. S.; Chan, H.-S. M.; Kang, S.; Lemay, S. G. Stochastic Amperometric Fluctuations as a Probe for Dynamic Adsorption in Nanofluidic Electrochemical Systems. *J. Am. Chem. Soc.* **2011**, *133*, 18289–18295.
16. Mampallil, D.; Mathwig, K.; Kang, S.; Lemay, S. G. Redox Couples with Unequal Diffusion Coefficients: Effect on Redox Cycling. *Anal. Chem.* **2013**, *85*, 6053–6058.

17. Lewis, P. M.; Sheridan, L. B.; Gawley, R. E.; Fritsch, I. Signal Amplification in a Microchannel from Redox Cycling with Varied Electroactive Configurations of an Individually Addressable Microband Electrode Array. *Anal. Chem.* **2010**, *82*, 1659–1668.
18. Fan, F. R. F.; Bard, A. J. Ultrathin Layer Cell for Electrochemical and Electron Transfer Measurements. *J. Am. Chem. Soc.* **1987**, *109*, 6262–6268.
19. Sun, P.; Mirkin, M. V. Electrochemistry of Individual Molecules in Zeptoliter Volumes. *J. Am. Chem. Soc.* **2008**, *130*, 8241–8250.
20. Fan, L.; Liu, Y.; Xiong, J.; White, H. S.; Chen, S. Electron-Transfer Kinetics and Electric Double Layer Effects in Nanometer-Wide Thin-Layer Cells. *ACS Nano* **2014**, *8*, 10426–10436.
21. Ma, C.; Contento, N. M.; Bohn, P. W. Redox Cycling on Recessed Ring-Disk Nanoelectrode Arrays in the Absence of Supporting Electrolyte. *J. Am. Chem. Soc.* **2014**, *136*, 7225–7228.
22. Cao, Z.; Peng, Y.; Voth, G. A. Ion Transport through Ultrathin Electrolyte under Applied Voltages. *J. Phys. Chem. B* **2015**, *119*, 7516–7521.
23. Bard, A. J.; Faulkner, L. R. *Electrochemical Methods: Fundamentals and Applications*, 2nd ed.; John Wiley & Sons: New York, 2001.
24. Martin, R. D.; Unwin, P. R. Scanning Electrochemical Microscopy: Theory and Experiment for the Positive Feedback Mode with Unequal Diffusion Coefficients of the Redox Mediator Couple. *J. Electroanal. Chem.* **1997**, *439*, 123–136.
25. Weaver, M. J. Potentials of Zero Charge for Platinum-(111)−Aqueous Interfaces: A Combined Assessment from In-Situ and Ultrahigh-Vacuum Measurements. *Langmuir* **1998**, *14*, 3932–3936.
26. Nioradze, N.; Chen, R.; Kurapati, N.; Khvataeva-Domanov, A.; Mabic, S.; Amemiya, S. Organic Contamination of Highly Oriented Pyrolytic Graphite As Studied by Scanning Electrochemical Microscopy. *Anal. Chem.* **2015**, *87*, 4836–4843.
27. White, H. S.; Leddy, J.; Bard, A. J. Polymer Films on Electrodes. 8. Investigation of Charge-Transport Mechanisms in Nafion Polymer Modified Electrodes. *J. Am. Chem. Soc.* **1982**, *104*, 4811–4817.
28. Sparreboom, W.; Eijkel, J. C. T.; Bomer, J.; van den Berg, A. Rapid Sacrificial Layer Etching for the Fabrication of Nanochannels with Integrated Metal Electrodes. *Lab Chip* **2008**, *8*, 402–407.